LASER
& PHOTONICS
REVIEWS

Laser Photonics Rev. **9,** No. 6, 650–655 (2015) / **DOI** 10.1002/lpor.201500058

ORIGINAL
PAPER

Abstract Plasmon resonances in nanopatterned single-layer graphene nanoribbons (SL-GNRs), double-layer graphene nanoribbons (DL-GNRs) and triple-layer graphene nanoribbons (TL-GNRs) are studied experimentally using 'realistic' graphene samples. The existence of electrically tunable plasmons in stacked multilayer graphene nanoribbons was first experimentally verified by infrared microscopy. We find that the strength of the plasmonic resonance increases in DL-GNRs when compared to SL-GNRs. However, further increase was not observed in TL-GNRs when compared to DL-GNRs. We carried out systematic full-wave simulations using a finite-element technique to validate and fit experimental results, and extract the carrier-scattering rate as a fitting parameter. The numerical simulations show remarkable agreement with experiments for an unpatterned SLG sheet, and a qualitative agreement for a patterned graphene sheet. We conclude with our perspective of the key bottlenecks in both experiments and theoretical models.

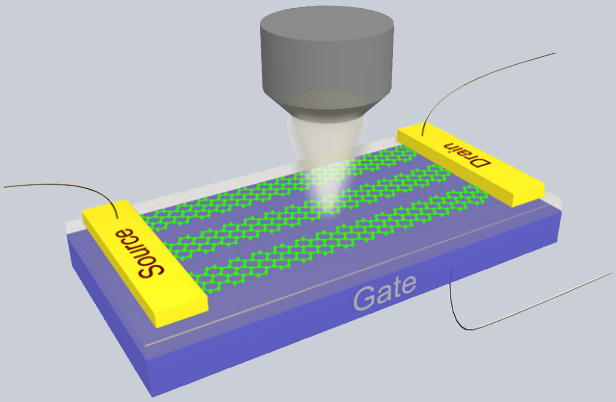

Plasmon resonance in multilayer graphene nanoribbons

Naresh Kumar Emani[1,3], Di Wang[1,3], Ting-Fung Chung[2,3], Ludmila J. Prokopeva[1,4], Alexander V. Kildishev[1,3], Vladimir M. Shalaev[1,3], Yong P. Chen[1,2,3], and Alexandra Boltasseva[1,3,5,*]

1. Introduction

Graphene has emerged as a versatile and dynamic platform for hybrid nanophotonics and optoelectronics due to its excellent electrical and optical properties [1–4]. This material has recently been integrated with metamaterials [5], plasmonic nanoanteannas [6–11], waveguides [12] and photonic crystals [13, 14] to realize electrically tunable hybrid devices. Nanostructured graphene has been shown to support highly confined surface plasmons with plasmon wavelengths 40–100 times smaller than the free-space wavelength at mid-infrared wavelengths [15–18]. These plasmon modes in graphene can be electrically controlled and have tremendous potential for confining and manipulating radiation for mid-infrared applications [15–17, 19, 20]. At present, there are two main challenges in the area of graphene plasmonics – to drive the plasmonic resonance to near-infrared wavelengths, and to increase the relatively small strength of the plasmon resonance, which is due to the finite optical conductivity of single-layer graphene (SLG) [21]. Optical studies of AB-stacked bilayer graphene using a synchrotron light source reveal that the optical conductivity of multilayer graphene is higher than SLG [22]. While the optical conductivity of SLG is consistent with the prediction of the random phase approximation (RPA) theory [4, 23], the spectrum of AB-stacked bilayer graphene shows an additional sharp resonance at 0.37 eV due to strong interlayer coupling [22]. Theoretical studies also predict such an enhanced optical conductivity in bilayer graphene due to strong interlayer coupling [24]. If the number of graphene layers is further increased the optical conductivity spectrum becomes progressively more complex, but the general trend of increasing optical conductivity is maintained [22]. On the other hand, carrier mobility, which determines the loss of the plasmonic resonance, decreases when the number of layers is increased due to modification of the electronic bandstructure. Until now, studies in graphene plasmonics have focused on SLG, which can be synthesized into large-area samples with reasonable ease. Due to enhanced optical conductivity, multilayer graphene could support stronger plasmonic resonances as compared to SLG. Furthermore, in multilayer graphene a perpendicular electric field could be applied to achieve stronger control on the plasmonic resonance [25]. In this paper we present our experimental and numerical studies on plasmon resonances in 'realistic' randomly stacked multilayer chemical vapor deposition (CVD) grown graphene nanoribbons (GNRs).

[1] School of Electrical and Computer Engineering, Purdue University, West Lafayette, IN 47907, USA
[2] Department of Physics and Astronomy, Purdue University, West Lafayette, IN 47907, USA
[3] Birck Nanotechnology Center, Purdue University, West Lafayette, IN 47907, USA
[4] Novosibirsk State University, Novosibirsk, Russia
[5] DTU Fotonik, Department of Photonics Engineering, Technical University of Denmark, Lyngby, DK-2800, Denmark
*Corresponding author: e-mail: aeb@purdue.edu

2. Experiment

We transfer and stack CVD-grown SLG sheets to form multilayer graphene samples due to difficulties in obtaining large-area samples with controlled number of layers by mechanical exfoliation. SLG was first grown on 25-μm thick Cu foils using an atmospheric pressure CVD process [26–28]. It was then sequentially transferred assisted by poly(methyl methacrylate) (PMMA) [26, 29] on three separate silicon substrates (1–10 Ohm cm) with 300 nm of thermal oxide (Si/SiO_2) to form single-layer, double-layer, and triple-layer devices. Subsequently, a 500 μm × 500 μm active area was defined by photolithography and oxygen plasma etching. The source–drain contacts were defined by photolithography and subsequent Ti and Au metallization (5 nm and 55 nm, respectively) on each sample.

It is well known that the layer-stacking order in multilayer graphene plays a crucial role in determining its optical properties [30]. In our samples the domain orientation is not uniform across the graphene layer and there is also no definite stacking order between adjacent layers. Hence, the optical response will be averaged over many domains with random orientations in a large area. We performed Raman spectroscopy (532 nm, circularly polarized laser with ~1 μm spot size and 1 mW incident power on the sample) to probe local layer orientations in our samples, since it has been shown to be a sensitive probe of the unique electronic and phonon band structures in graphene layers [31]. From the Raman spectra (shown in Figs. 1a–c) we clearly observe that the I_{2D}/I_G ratio is dependent on the measurement location in double-layer and triple-layer graphene samples in contrast to the single-layer sample. This is due to changes in local lattice stacking order, which is consistent with previous studies in misoriented graphene [30, 32]. Hence, we should note that there is significant inter-layer stacking misalignment in addition to the well-known intralayer domain misalignment in CVD graphene samples. Electrical testing of the devices was also carried out to verify the gate modulation of the source–drain sheet resistance in multilayer graphene sheets. We found that SLG exhibits the highest dynamic range of variation of electrical resistance as shown in Fig. 1d, followed by double-layer graphene and triple-layer graphene, respectively. The gate-induced carrier-density modulation will allow multilayer GNRs to support tunable plasmonic resonances. The strength of such resonances would be strongly dependent on the optical conductivity and carrier mobility.

The active area was patterned into GNRs (50-nm width and 150-nm period) using electron beam lithography on a positive electron beam resist (ZEP 520A, Zeon Chemicals, Inc). Figure 2 shows a simplified schematic illustration of our experimental setup as well as a scanning electron micrograph showing the patterned graphene ribbons. The number of broken C–C bonds increases significantly in nanopatterned graphene in comparison to unpatterned large-area graphene, which leads to an additional peak (~1350 cm^{-1}) in the Raman spectra (see supplementary online material (SOM) Figure S4 for an example for SLG). However, we should note that even after patterning the I_{2D}/I_G ratio of

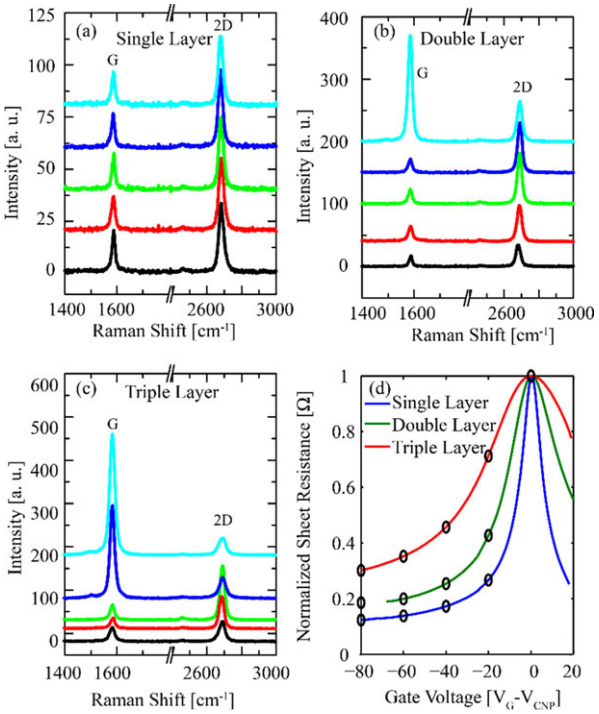

Figure 1 (a–c) Raman spectra collected from five random locations on single-layer, double-layer and triple-layer graphene, respectively. All the measurements were performed using a 532-nm, circularly polarized laser source with a 100× objective (spot size ~1 μm) and 1 mW incident power. Individual spectra are offset for clarity. (d) The gate modulation of source–drain resistance (normalized using sheet resistance at the charge-neutral point (CNP) voltage) in different samples. SLG exhibits the highest dynamic range of variation of electrical resistance followed by double-layer and triple-layer graphene, respectively. The open circles represent the gate voltages at which IR reflection data shown later is collected.

SLG is greater than 2, indicating that the physical properties of graphene are intact. To investigate the plasmonic resonance in GNRs we measure the IR reflectance, which we normalize to the reflectance at charge-neutral point (CNP). The optical measurements were performed using a Fourier transform infrared (FTIR) spectrometer (Nicolet Magna-IR 850) with a microscope accessory (Nicplan IR Scope, 15×, NA 0.58 Reflectochromat objective). The incoming beam was polarized with the electric field perpendicular to ribbons using a wire grid polarizer to excite transverse magnetic modes in GNRs.

When graphene is patterned into nanoribbons it can support surface plasmon standing waves when the condition $\mathrm{Re}(\beta)W = m\pi + \phi$ is satisfied, where β is the surface plasmon propagation constant, W is the width of the GNR, and ϕ is an arbitrary phase shift introduced by the reflection at the GNR edge and m is an integer [15, 18, 33]. Plasmon resonances in 50-nm wide GNRs occur in the wavelength range of 7–10 μm when graphene is doped to 1×10^{12} – 7×10^{12} cm^{-2} carrier densities. The experimental measurements of normalized reflectance on SL-GNRs, DL-GNRs

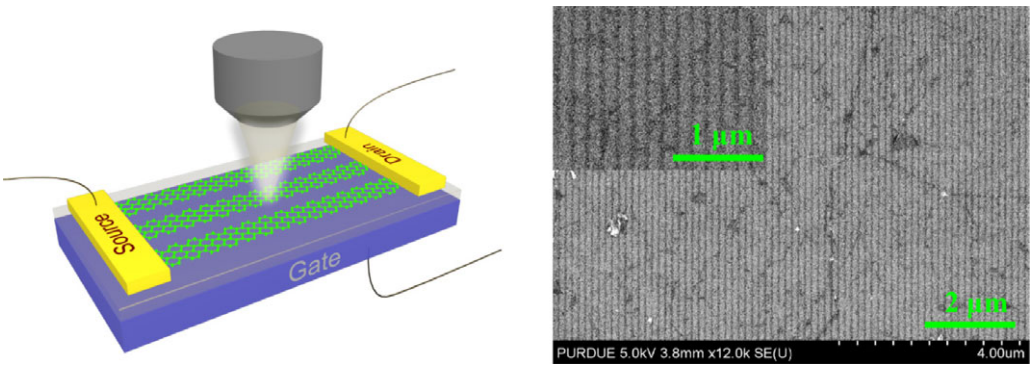

Figure 2 (a) Simplified schematic of the experimental setup used for studying plasmon resonance in GNRs. The lattice orientation of GNRs in the figure is for illustration only and dimensions are not to scale; (b) Scanning electron micrograph of the fabricated GNRs on a SLG sample with the inset showing a zoomed-in view of GNRs.

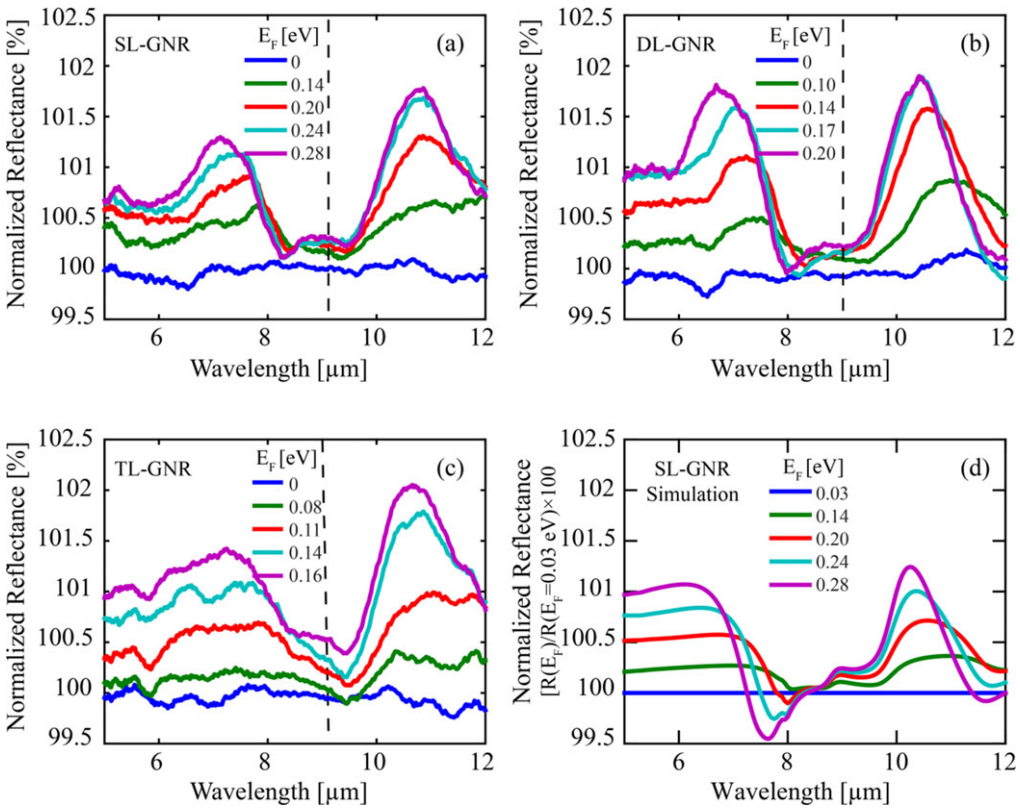

Figure 3 Modulation of IR reflectivity of GNRs fabricated on Si/SiO_2 substrate as a function of Fermi energy (E_F) of graphene; the vertical dashed line indicates the peak of the SiO_2 optical phonon. Panels (a)–(c) show measured data on SL-GNRs, DL-GNRs and TL-GNRs, respectively. The reflection measurements were normalized to the reflection at the charge-neutral point in our experiments. The width and period of GNRs were fixed at 50 nm and 150 nm, respectively. (d) 2D full-wave FEFD simulations of SL-GNRs with COMSOL Multiphysics using a surface current model for graphene; simulations performed at 0° to 35° angles of incidence (φ) with 5° spacing were averaged to obtain the curves shown here (see SOM on substrate characterization for further details). The Fermi energy for each sample was calculated using a uniform charge approximation that does not take into account the screening and interlayer coupling effects (see SOM Section 6 for further details).

and TL-GNRs as a function of Fermi energy E_F (which is related to the carrier density, see SOM Section 6) are shown in Fig. 3. As the carrier density in GNRs is increased the plasmon resonance becomes stronger and moves to shorter wavelengths. There are two main peaks observed in the measured data – one above and another below the optical phonon wavelength of SiO_2. These peaks result from hybridization of the graphene plasmon with the optical phonon in the SiO2 layer [15, 18, 34]. The resonance strength increases from SL-GNRs to DL-GNRs, but the increase is

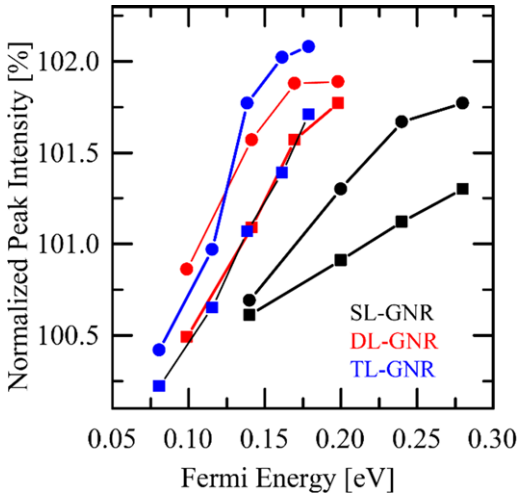

Figure 4 Peak intensity of the resonance peaks shown in Fig. 3 as a function of E_F. The graphene plasmon hybridizes with the SiO_2 optical phonon to give two peaks shown by square and circle markers, respectively. Square markers indicate resonance peaks at shorter wavelengths, while circles indicate resonance peaks at longer wavelengths.

slightly less for TL-GNRs. This could be due to higher losses resulting from the increase in the number of defects arising out of stacking multiple layers.

In Figure 4 we plot the peak intensities of the resonance peaks shown in Fig. 3 as a function of Fermi energy. We find that the peak resonance intensities in DL-GNRs are significantly stronger than SL-GNRs at a fixed E_F. When E_F is held constant the total carrier concentration of the stack is simply the carrier concentration in SL-GNRs times the number of graphene layers. We should note that a similar strong increase in peak intensity of TL-GNRs is not seen when compared to DL-GNRs. We believe that this could be due to the fact that the PMMA-assisted transfer of CVD graphene invariably creates some holes, folds and unavoidable residue. In fact, as we increase the number of layers the nonuniformities become quite apparent in SEM images (see Fig. 2b for a representative image of SL-GNRs) and even under an optical microscope. Therefore, we believe that this increase in number of defects per unit area leads to progressively higher losses, and weaker response that manifests as broadening of the plasmon peak in Figs. 3a–c. While the quality of our samples is comparable to the current state of the art in CVD graphene, we can expect that further improvements in graphene growth/transfer processes will help in further enhancing the plasmon resonance strength.

3. Numerical simulations

To gain further insight into the experiments we performed full-wave finite-element frequency-domain (FEFD) simulations using a commercial software package (COMSOL Multiphysics, Wave Optics Module). We first accurately determined the dielectric function of SiO_2, which has a strong optical phonon overlapping with the graphene plasmon [15, 34], using IR spectroscopic ellipsometry. The retrieved optical constants for Si and SiO_2 layers are used in subsequent simulations and are shown in Fig. S1. The optical properties of graphene were calculated using the local limit of the random phase approximation (RPA) and were modeled as a surface current in FEFD simulations.

The surface current model in COMSOL was first validated for an unpatterned single graphene sheet on SiO_2/Si substrate by modifying the classical Drude equation for the complex reflection coefficient [35], now rewritten as $r = (r_{01}^{\pm} + r_{01}^{\mp} r_{12} e^{\imath 2k_1\delta})/(1 + r_{01}^{=} r_{12} e^{\imath 2k_1\delta})$. The classical Fresnel coefficient for p-polarized light, $r_{12} = (\varepsilon_2 k_1 - \varepsilon_1 k_2)/(\varepsilon_2 k_1 + \varepsilon_1 k_2)$, was still applicable at the second interface with no graphene sheet, with $k_i = \frac{\omega}{c}\sqrt{\varepsilon_i - \varepsilon_0 \sin^2\varphi}$, $i \in \overline{0,2}$ for a given frequency of light ω and angle of incidence φ. While using $\xi = \sigma k_0 k_1/(\omega\varepsilon_0)$ three different permutations of a modified Fresnel coefficient at the first interface, $r_{01}^{\pm} = (\varepsilon_1 k_0 + \xi - \varepsilon_0 k_1)/(\varepsilon_1 k_0 + \xi + \varepsilon_0 k_1)$, $r_{01}^{\mp} = (\varepsilon_1 k_0 - \xi + \varepsilon_0 k_1)/(\varepsilon_1 k_0 + \xi + \varepsilon_0 k_1)$, and $r_{01}^{=} = (\varepsilon_1 k_0 - \xi - \varepsilon_0 k_1)/(\varepsilon_1 k_0 + \xi + \varepsilon_0 k_1)$, were required to account for the effect of the graphene layer. Here, $\varepsilon_0, \varepsilon_1, \varepsilon_2$ are the dielectric constants of air, SiO_2 and Si substrate, and σ, δ, and c are the conductivity of the graphene layer, the thickness of silicon dioxide and the free-space speed of light respectively. Further details of our implementation and can be found in SOM.

We found that simulations at only normal incidence do not fully account for all the experimental features (see SOM Fig. S2). Therefore, we developed a weighted averaging procedure where the contribution of each simulation performed with 0° to 35° angles of incidence was weighted with a Gaussian factor. The upper limit of 35° was chosen to account for the finite acceptance angle of the objective used in our experiment. The final results thus obtained capture the experimental data remarkably well as compared to just normal reflectance, as shown in Fig. S2. From this analysis we retrieved a carrier-scattering time of ~10 fs for the unpatterned graphene sample that is 5 times lower than the value estimated using DC Drude model [3] (see SOM Sections 2 and 6 for additional details). We also recently became aware of another study that reports an experimentally extracted scattering time of 18 fs, which is in the same range as our results [36]. In numerical simulations SL-GNRs were modeled as a patterned surface current. The results obtained with the averaging procedure described above are shown in Fig. 3d, where we see a qualitative agreement with the experimental results. A key difference is the considerably narrower plasmon peaks below the SiO_2 optical phonon wavelength in experiments when compared to simulations. When graphene is patterned into nanoribbons the carriers are confined to a 1D strip leading to opening of an energy bandgap. At the same time there is also significant edge disorder leading to charge localization and a smaller effective width of the GNR [37]. The bandgap (E_{gap}) is found to be empirically related to the GNR width (W) and disorder parameter (W^*) as $E_{gap} = \alpha/(W - W^*)$ based on

electrical-transport studies on epitaxial graphene [37]. According to these studies a rather large bandgap of 0.2 eV can be obtained for GNR widths of ∼15 nm. It seems plausible that such a bandgap could reduce the optical loss at IR wavelengths, and consequently lead to narrower plasmon resonance peaks. While we can expect significant differences between electrical and optical responses, it seems plausible that such a bandgap could reduce the optical loss at IR wavelengths. Based on our numerical studies we conclude that the experimental features cannot be attributed to variations in the width of the ribbons or carrier-scattering time alone. Therefore, we believe that the optical conductivity for graphene ribbons should be rederived taking into account the energy bandgap, which is beyond the scope of this work.

4. Conclusions and outlook

A major current challenge in the area of graphene plasmonics is to improve the strength of the plasmonic resonance. CVD-grown graphene, which yields large sample area, has been predominantly used in graphene plasmon studies due to the ease of optical characterization. However, growth kinetics and the transfer method of CVD graphene lead to disorder and hence poorer physical properties compared to epitaxial graphene films on silicon carbide. We investigated the behavior of plasmon resonance in GNR in single-layer and multilayer 'realistic' CVD graphene. Our experimental results indicate that plasmons are indeed supported by multilayer graphene nanostructures. When the carrier concentration of the graphene sheet is fixed, we find that DL-GNRs show stronger plasmon peaks when compared to SL-GNRs. However, the increase is weak from DL-GNRs to TL-GNRs most likely due to inhomogeneities in local stacking order as well as random orientation of domains within CVD graphene. Systematic numerical simulations were performed in order to obtain a very good fit with experimental results for unpatterned graphene. Thus, we retrieved a carrier-scattering time of ∼10 fs from our graphene sample and developed an accurate numerical model that takes into account contributions from 0° to 35° incidence angles. The developed simulation model was applied for GNRs, and the results agree qualitatively with the experiment, but show broader plasmonic resonances. We believe that this could be due to opening of the bandgap close to the Dirac point due to nanopatterning. While incorporating a bandgap into the numerical model could theoretically lead to a better fit, we believe that such advanced modeling would first require better-quality graphene samples and accurate measurements.

Funding Sources

The authors want to acknowledge financial support from ARO MURI Grant 56154-PH-MUR (W911NF-09-1-0539) and NSF Materials Research Science and Engineering Center (MRSEC) program DMR1120923. The graphene synthesis and Raman characterization were supported by NSF DMR 0847638.

Supporting Information

Additional supporting information may be found in the online version of this article at the publisher's website.

Acknowledgements. The authors thank Dr. Tom Tiwald (J. A. Woollam Co.) for performing the IR spectroscopic ellipsometry of the substrates used in this work, and a very useful discussion on substrate phonon characterization. We also thank Clayton DeVault and Rohith Chandrasekar for assistance with preparation of the manuscript.

Abbreviations

CVD	Chemical Vapor Deposition
SLG	Single-Layer Graphene
GNRs	Graphene Nanoribbons
SL-GNRs	Single-Layer GNRs
DL-GNRs	Double-Layer GNRs
TL-GNRs	Triple-Layer GNRs
CNP	Charge-Neutral Point
FTIR	Fourier Transform Infrared Spectroscopy

Received: 11 March 2015, **Revised:** 25 June 2015,
Accepted: 24 September 2015

Published online: 26 October 2015

Key words: Graphene plasmonics, multilayer CVD graphene, plasmon–substrate phonon interaction.

References

[1] F. Bonaccorso, Z. Sun, T. Hasan, and A. Ferrari, Nature Photon. **4**, 611–622 (2010).
[2] A. K. Geim and K. S. Novoselov, Nature Mater. **6**, 183–191 (2007).
[3] F. J. García de Abajo, ACS Photon. **1**, 135–152 (2014).
[4] F. H. L. Koppens, D. E. Chang, and F. J. Garcia de Abajo, Nano Lett. **11**, 3370–3377 (2011).
[5] N. Papasimakis, Z. Luo, Z. X. Shen, F. De Angelis, E. Di Fabrizio, A. E. Nikolaenko, and N. I. Zheludev. Opt. Exp. **18**, 8353–8359 (2010).
[6] N. K. Emani, T.-F. Chung, X. Ni, A. V. Kildishev, Y. P. Chen, and A. Boltasseva. Nano Lett. **12**, 5202–5206 (2012).
[7] N. K. Emani, T.-F. Chung, A. V. Kildishev, V. M. Shalaev, Y. P. Chen, and A. Boltasseva. Nano Lett. **14**, 78–82 (2013).
[8] Y. Yao, R. Shankar, M. Kats, Y. Song, J. Kong, M. Loncar, and F. Capasso. Nano Lett. **14**, 6526–6532 (2014).
[9] Y. Yao, M. A. Kats, R. Shankar, Y. Song, J. Kong, M. Loncar, and F. Capasso. Wide Nano Lett. **14**, 214–219 (2013).
[10] S. H. Mousavi, I. Kholmanov, K. B. Alici, D. Purtseladze, N. Arju, K. Tatar, D. Y. Fozdar, J. W. Suk, Y. Hao, A. B. Khanikaev, et al. Nano Lett. **13**, 1111–1117 (2013).

[11] J. Kim, H. Son, D. J. Cho, B. Geng, W. Regan, S. Shi, K. Kim, A. Zettl, Y.-R. Shen, and F. Wang. Nano Lett. **12**, 5598–5602 (2012).
[12] M. Liu, X. Yin, E. Ulin-Avila, B. Geng, T. Zentgraf, L. Ju, F. Wang, and X. Zhang. Nature **474**, 64–67 (2011).
[13] A. Majumdar, J. Kim, J. Vuckovic, and F. Wang. Nano Lett. **13**, 515–518 (2013).
[14] X. Gan, K. F. Mak, Y. Gao, Y. You, F. Hatami, J. Hone, T. F. Heinz, and D. Englund. Nano Lett. **12**, 5626–5631 (2012).
[15] V. W. Brar, M. S. Jang, M. Sherrott, J. J. Lopez, and H. A. Atwater. Nano Lett. **13**, 2541–2547 (2013).
[16] Z. Fei, A. S. Rodin, G. O. Andreev, W. Bao, A. S. McLeod, M. Wagner, L. M. Zhang, Z. Zhao, M. Thiemens, G. Dominguez, et al. Nature **487**, 82–85 (2012).
[17] J. Chen, M. Badioli, P. Alonso-Gonzalez, S. Thongrattanasiri, F. Huth, J. Osmond, M. Spasenovic, A. Centeno, A. Pesquera, P. Godignon, et al. Nature **487**, 77–81 (2012).
[18] H. Yan, T. Low, W. Zhu, Y. Wu, M. Freitag, X. Li, F. Guinea, P. Avouris, and F. Xia. Nature Photon. **7**, 394–399 (2013).
[19] Z. Fang, S. Thongrattanasiri, A. Schlather, Z. Liu, L. Ma, Y. Wang, P. M. Ajayan, P. Nordlander, N. J. Halas, and F. J. García de Abajo. ACS Nano **7**, 2388–2395 (2013).
[20] Z. Fang, Y. Wang, A. E. Schlather, Z. Liu, P. M. Ajayan, F. J. Garcia de Abajo, P. Nordlander, X. Zhu, and N. J. Halas. Nano Lett. **14**, 299–304 (2013).
[21] K. F. Mak, M. Y. Sfeir, Y. Wu, C. H. Lui, J. A. Misewich, and T. F. Heinz. Phys. Rev. Lett. 2008, **101**:196405.
[22] K. F. Mak, M. Y. Sfeir, J. A. Misewich, and T. F. Heinz. Proc. Natl. Acad. Sci. **107**, 14999–15004 (2010).
[23] L. Falkovsky and S. Pershoguba. Phys. Rev. B 2007, **76**:153410.
[24] A. Wright, J. Cao, and C. Zhang. Phys. Rev. Lett. 2009, **103**:207401.
[25] Y. Zhang, T.-T. Tang, C. Girit, Z. Hao, M. C. Martin, A. Zettl, M. F. Crommie, Y. R. Shen, and F. Wang. Nature **459**, 820–823 (2009).
[26] T. F. Chung, T. Shen, H. Cao, L. A. Jauregui, W. Wu, Q. Yu, D. Newell, and Y. P. Chen. Intl. J. Mod. Phys. B 2013, **27**.
[27] Q. Yu, L. A. Jauregui, W. Wu, R. Colby, J. Tian, Z. Su, H. Cao, Z. Liu, D. Pandey, and D. Wei. Nature Mater. **10**, 443–449 (2011).
[28] H. Cao, Q. Yu, L. A. Jauregui, J. Tian, W. Wu, Z. Liu, R. Jalilian, D. K. Benjamin, Z. Jiang, and J. Bao. Appl. Phys. Lett. 2010, **96**:122106.
[29] N. Petrone, C. R. Dean, I. Meric, A. M. Van Der Zande, P. Y. Huang, L. Wang, D. Muller, K. L. Shepard, and J. Hone. Nano Lett. **12**, 2751–2756 (2012).
[30] K. Kim, S. Coh, L. Z. Tan, W. Regan, J. M. Yuk, E. Chatterjee, M. Crommie, M. L. Cohen, S. G. Louie, and A. Zettl. Phys. Rev. Lett. 2012, **108**:246103.
[31] A. C. Ferrari and D. M. Basko. Nature Nanotechnol. **8**, 235–246 (2013).
[32] R. W. Havener, H. Zhuang, L. Brown, R. G. Hennig, and J. Park. Nano Lett. **12**, 3162–3167 (2012).
[33] M. Jablan, H. Buljan, and M. Soljacic. Phys. Rev. B **80**, 245435 (2009).
[34] X. Zhu, W. Wang, W. Yan, M. B. Larsen, P. Bøggild, T. G. Pedersen, S. Xiao, J. Zi, and N. A. Mortensen. Nano Lett. **14**, 2907–2913 (2014).
[35] P. Drude. Ann. Phys. **272**, 865–897 (1889).
[36] N. Dabidian, I. Kholmanov, A. B. Khanikaev, K. Tatar, S. Trendafilov, S. H. Mousavi, C. Magnuson, R. S. Ruoff, and G. Shvets. ACS Photon. **2**, 216–227 (2015).
[37] M. Y. Han, B. Ozyilmaz, Y. Zhang, and P. Kim. Phys. Rev. Lett. **98**, 206805 (2007).